Journal of Asian Earth Sciences 233 (2022) 105261

Contents lists available at ScienceDirect

Journal of Asian Earth Sciences

journal homepage: www.elsevier.com/locate/jseaes

Moho depth and crustal density structure in the Tibetan Plateau from gravity data modelling

Songbai Xuan [a], Shuanggen Jin [a,b,*]

[a] Shanghai Astronomical Observatory, Chinese Academy of Sciences, Shanghai 200030, China
[b] School of Surveying and Land Information Engineering, Henan Polytechnic University, Jiaozuo 454000, China

ARTICLE INFO

Keywords:
Regional gravity anomaly
Local gravity anomaly
Moho depth
Density structure
Tibet

ABSTRACT

Although a large number of geophysical experiments have been performed in the Tibetan plateau and its surroundings, our knowledge and understanding of the uplift and deformation in the Tibetan Plateau caused by the India-Asia collision is still incomplete. Gravity method is inevitable and indispensable tool to investigate the evolution of the Tibetan Plateau due to the environmental complexity. In this study, images of the Moho depth and density disturbances in the Tibetan plateau are derived from the separated regional and local gravity anomalies, respectively. The results show that the Moho depth and density present distinct change from north to south in the central and western Tibetan Plateau, but both are relatively featureless in the eastern region. Moho depth sublinearly increases from the south to north and exceed 70 km at the Bangong-Nujiang suture, interpreted as the downward bending of the Tibetan crust due to the subductions of the Indian plate to the south and Asian plate to the north. The significant low density occurs in the middle and lower crust beneath Himalayas, suggesting the absence of the eclogites under the fast subducting effect of the cold Indian plate. In contrast, the high density may suggest the probable presence of eclogites underneath the Lhasa and Qiangtang terranes, where the mantle convection and thickened crust would provide environment of the high temperatures and pressures for eclogite formation. Low density presents underneath the Jinsha suture, indicating that the partial melting occurs due to the upwelling of asthenospheric material.

1. Introduction

The India-Asia collision began at ~50 Ma and resulted in the uplift of the Himalayas and the Tibetan Plateau (Molnar and Tapponnier, 1975; Yin and Harrison, 2000). With an average elevation of 4–5 km and ~70 km thick crust (Li et al., 2006; Li et al., 2014; Teng et al., 2013, 2020), the Tibetan Plateau is an unparalleled region for studying the mechanics of continental deformation. Four bordering sutures, i.e., the Indus-Yalu suture (IYS), the Bangong-Nujiang suture (BNS), the Jinshajiang suture (JS), and the Anyimaqen-Kunlun-Mutztagh suture (AKMS), separate the Tibetan Plateau into the Himalaya Mountains (HM), the Lhasa terrane (LT), the Qiangtang terrane (QT), the Songpan-Ganzi terrane (ST), and the Kunlun-Qilian terrane (KT) (Yin and Harrison, 2000; Zhu et al., 2013). Over the last few decades, several geophysical and geodetic investigations have been conducted in geodynamics (Jin and Park, 2006; Jin et al. 2011, Tenzer et al., 2015) and abundant tectonic activities beneath the Tibetan Plateau have been studied (Bai et al., 2013; Bao et al., 2015; He et al., 2010; Hetényi et al., 2007; Huang and Zhao, 2006; Jiménez-Munt et al., 2008; Jin et al., 2010; Kumar et al., 2006; Li et al., 2008; Liang et al., 2016; Nábělek et al., 2009; Owens and Zandt, 1997; Teng et al., 2020; Wang et al., 2003; Wang et al., 2019; Zhang et al., 2014; Zhao et al., 2013; Zhao et al., 2020; Zheng et al., 2007). However, the long-standing question on the tectonic mechanism responsible for the crustal thickening and uplift in the Tibetan Plateau caused by the India-Asia collision is still debated, and several remarkable models have been proposed, including internal deformation (Houseman and England, 1986), block extrusion (Tapponnier et al., 1982), and lower crustal flow (Clark and Royden, 2000; Royden et al., 1997). Additionally, several arguments exist for the underthrusting distance of the Indian Plate, i.e., to the BNS (Tilmann et al., 2003), to the central QT (Owens and Zandt, 1997), and to north margin of the QT (Huang and Zhao, 2006; Zheng et al., 2007).

The Moho topography and density structure provide important clues for understanding the tectonic evolution of the Tibetan Plateau (Bai et al., 2013; Hetényi et al., 2007; Jiménez-Munt et al., 2008; Zhang et al., 2014). Gravity modeling for investigations of the crustal structure

* Corresponding author at: Shanghai Astronomical Observatory, Chinese Academy of Sciences, Shanghai 200030, China.
E-mail address: sgjin@shao.ac.cn (S. Jin).

https://doi.org/10.1016/j.jseaes.2022.105261
Received 2 July 2020; Received in revised form 25 April 2022; Accepted 2 May 2022
Available online 6 May 2022

has a distinct advantage in the inaccessible regions of the Tibetan Plateau. Although previous studies have reported the Moho undulation (Braitenberg et al., 2000; Shin et al., 2006, 2007; Xu et al., 2017; Zhao et al., 2020) and crustal density (Bai et al., 2013; Hetényi et al., 2007; Jiménez-Munt et al., 2008) in the Tibetan Plateau, simultaneous investigations of the Moho and crustal density structure using inverse modeling are rare. In this paper, the gravity anomaly, removing the effects of sediments and upper mantle from Bouguer anomaly, is separated into regional and local anomalies. The regional anomaly is used to determine the Moho depth following Deng et al (2014), and the local anomaly is applied to investigate the crustal density disturbances. The interactions between the Tibetan Plateau and the adjacent tectonic blocks are investigated, as well as the responses of the tectonic blocks to the lateral variations beneath the central part of the Tibetan Plateau.

2. Data and analysis

The Bouguer gravity anomaly with a spatial resolution of 0.1 × 0.1 arc-degree used in this study (Fig. 2), was generated from the WGM2012 model (Bonvalot et al., 2012), which is available at BGI (Bureau Gravimétrique International) website (https://bgi.obs-mip.fr/). This dataset, including 1′ × 1′ resolution terrain corrections using ETOPO1 model, is derived from the available Earth global gravity models EGM2008 and DTU10. The significant feature of the gravity anomaly is that the gradient belts are consistent with the major faults around the Tibetan and Pamir plateaus, i.e., the Main Boundary Thrust to the south, the Altyn Tagh fault to the north, and the Longmen Shan to the east. The positive anomaly with over 100 mGal covers the Indian Plate. The high negative anomaly is distributed across the Tibetan and Pamir plateaus. In particular, the −250 mGal contour is nearly consistent with the margin of the plateaus. In the Tian Shan region, the anomaly is approximately −200 mGal. Outward from the plateaus, to the east and north, the anomaly tends to −100 mGal, especially in the Sichuan and Tarim basins.

The densities of sediments in the Bay of Bengal, Ganges, Tarim and Sichuan basins are quite different from the crustal average density, as well as the subducting Indian and the Eurasian lithosphere are in the seismic velocities (Liang et al., 2016; Zhang et al., 2014). The gravity effects from the sediment basins and upper mantle should be taken into consideration before investigating the crustal structures.

2.1. Gravity effects from sediments

The sediments thickness from CRUST1.0 (Laske et al., 2013) and a sediment density of 2540 kg/m^3 are used to compute the gravity effects from the sediments. The thickness more than 5 km exists in the Bay of Bengal, Ganges, Tarim and Sichuan basins (Fig. 3a). Fig. 3b shows an anomaly of approximate −80 mGal in the Bay of Bengal, about −30 mGal in the Ganges basin, and exceeding −40 mGal in the Tarim and Sichuan basins.

2.2. Gravity effects from upper mantle

The relation between global shear-wave velocity (V_S) and the density anomaly, ($\Delta\rho$), can be given as (Levandowski et al., 2015; Deng et al., 2017):

$$\Delta V_S = 100 \times (V_S - V_0)/V_0; \tag{1a}$$

$$\Delta\rho = \Delta V_S\left(7.3 - \frac{z}{100} + \frac{\Delta V_S}{4}\right); \quad \Delta V_S \leqslant 6\% \tag{1b}$$

$$\Delta\rho = \Delta V_S\left(8.8 - \frac{z}{100} - \frac{7(\Delta V_S - 6)}{40}\right); \quad \Delta V_S > 6\% \tag{1c}$$

$$\Delta\rho = 0, \quad \Delta V_S \leqslant 0\% \tag{1d}$$

where, ΔV_S is the anomaly (in %) relative to V_0.

The *Vs* structure from Kustowski et al. (2008a, 2008b) was used here for deriving the density anomaly ($\Delta\rho$) from 50 to 200 km (Fig. 3). The V_S less than 4.5 km/s dominates depth range of 50–100 km underneath the Tibetan Plateau (Fig. 3a and 3b). The V_S around 4.7 km/s presents in the Indian Plate, Sichuan and Tarim basins (Fig. 3a-d). The V_S larger than 4.7 km/s exists in the depth range of 125–200 km in the Tibetan Plateau and Tian Shan region (Fig. 3d and 3e).

The density anomalies in the depth range of 50–200 km (Fig. 4a-e) were derived from the *Vs* structure based on Eq.(1) and assumed V_0 to be 4.5 km/s (Sato et al., 1989). Fig. 4f showed the gravity anomaly computed from the density anomaly. The gravity anomaly more than

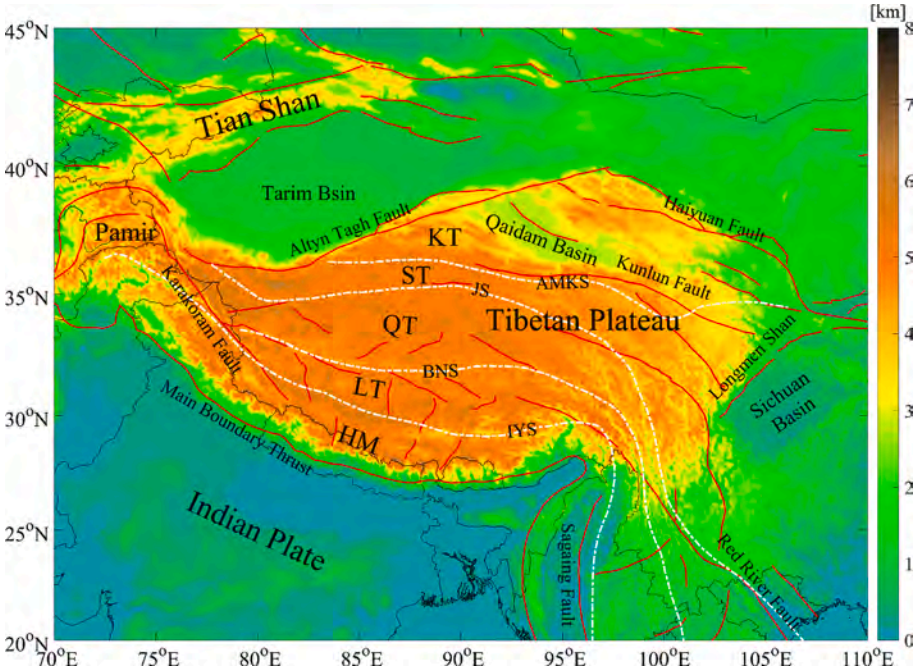

Fig. 1. Tectonic setting of the Tibetan Plateau overlying the topographic map. The red lines represent the major faults. The white dotted lines represent the sutures. *HM*, Himalaya Mountains; *LT*, Lhasa Terrane; *QT*, Qiangtang Terrane; *ST*, Songpan-Ganzi Terrane; *KT*, Kunlun Terrane; *IYS*, Indus-Yalu suture; *BNS*, Bangong-Nujiang suture; *JS*, Jinshajiang suture; *AMKS*, Anyimaqen-Kunlun-Mutztagh suture. (For interpretation of the references to colour in this figure legend, the reader is referred to the web version of this article.)

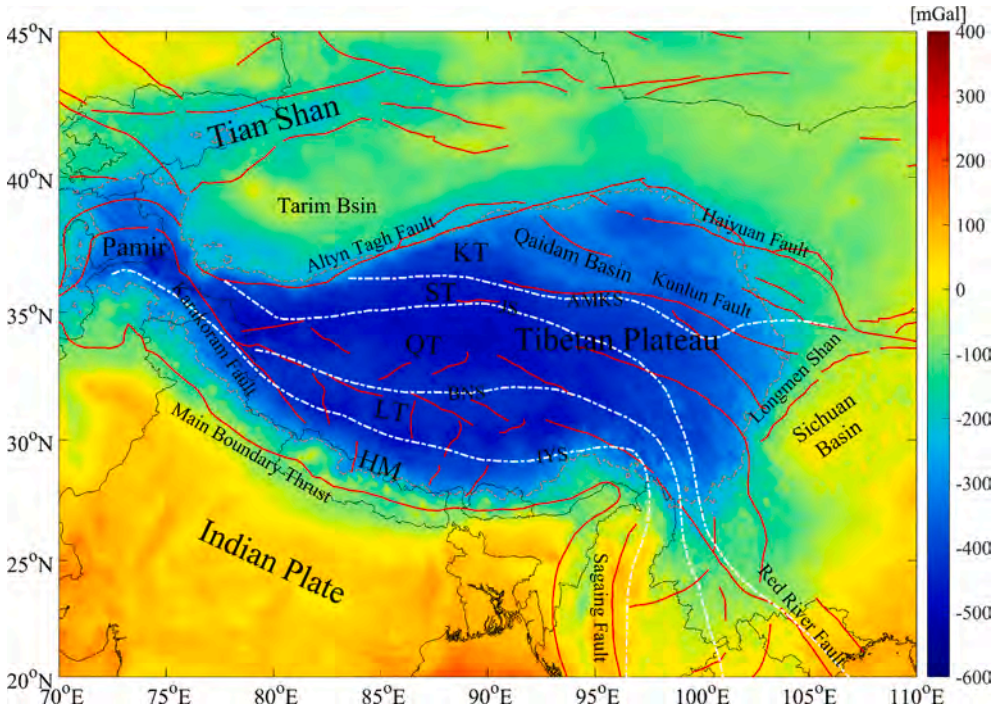

Fig. 2. Bouguer gravity anomaly in the Tibetan Plateau generated from WGM2012 (Bonvalot et al., 2012). The grey dotted lines represent the gravity anomaly of −250 mGal, which probably outlines the Tibetan and Pamir plateaus.

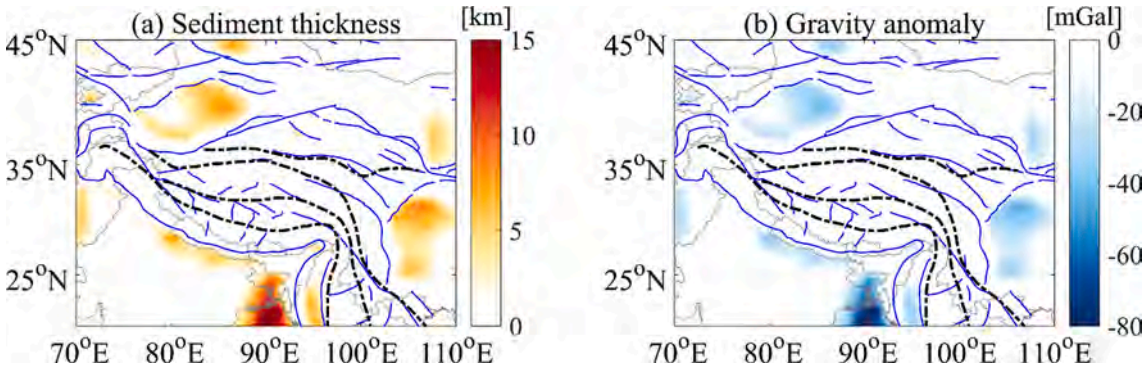

Fig. 3. (a) Sediment thickness and (b) its gravity effects in the Tibetan Plateau and its surroundings. Sediment thickness map from CRUST1.0 model (Laske et al., 2013).

100 mGal distributed in the Indian Plate, southern Tibetan Plateau, Tarim and Sichuan basins, especially in the southwestern Tibetan Plateau, the anomaly exceeded 200 mGal.

2.3. Gravity anomaly analysis

To determine the Moho depth and crustal density structure, we derived the corrected Bouguer gravity anomaly (CBGA) (Fig. 6a) after removing the gravity effects from the sediments and upper mantle (Fig. 3b and 5f) from the Bouguer gravity anomaly (Fig. 2). The significant feature of the CBGA is the gradient belts are consistent with the major faults around the Tibetan and Pamir plateaus, i.e., the Main Boundary Thrust to the south, the Altyn Tagh fault to the north, and the Longmen Shan to the east. The high negative anomaly distributes in the Tibetan and Pamir plateaus. In particular, the −250 mGal contour is nearly consistent with the margin of the plateaus. In the Tian Shan region, the anomaly is approximately −200 mGal. Outward from the plateaus, to the east and north, the anomaly tends to 0 mGal, especially in the Indian plate, Sichuan and Tarim basins.

The gravity anomaly is generally separated into regional and local anomalies before interpreting the data. We used the discrete wavelet transform method to further investigate the features of the CBGA. After testing wavelet decomposition with different orders, we present the spectral analysis of the fourth-order wavelet approximation (Fig. 7). The average source depth of 42.3 km, which agrees with the average continental crustal thickness, estimated by the relation between the wavenumber and logarithmic power spectral density. Thus, the fourth-order wavelet approximation can be considered as the regional anomaly for determining Moho depth. In turn, the local anomaly was assessed after removing the regional anomaly from the CBGA.

The regional anomaly (Fig. 6b) represents the gravity information with a wavelength greater than 90 km according to the investigation for the relation between the wavelength of the gravity anomaly and the wavelet orders (Yang et al., 2001). The regional map more clearly displays the gradient belts with sharp variations around the Tibetan and Pamir plateaus. However, the gravity anomaly (-200 mGal to 0 mGal) slowly extends to the southeastern margin for approximately 700 km, which is consistent with the slowly varying topography (Fig. 1). An

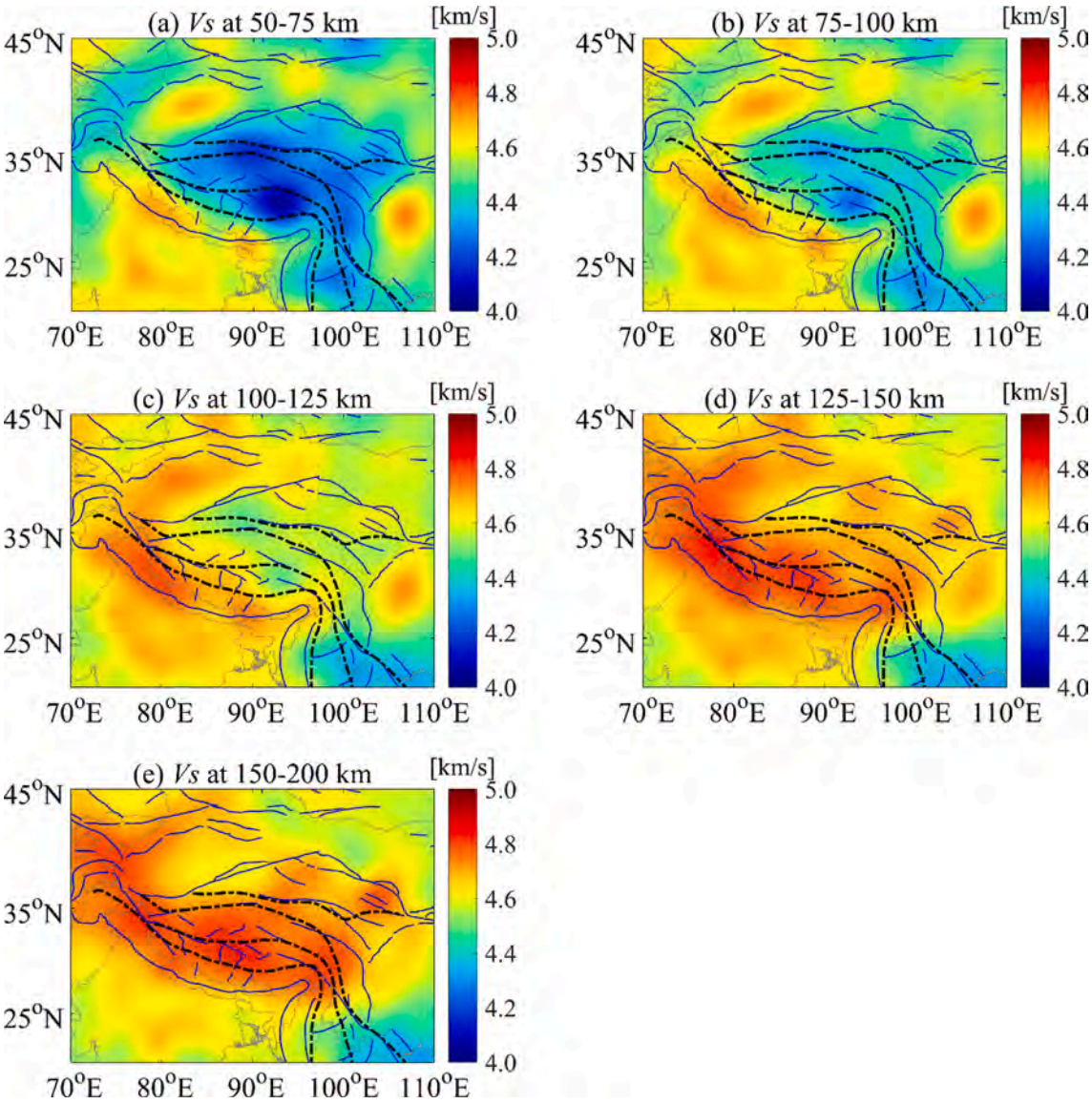

Fig. 4. Shear-wave velocity (V_s) from 50 to 200 km beneath the Tibetan Plateau and its surroundings.

extreme gravity high of greater than −500 mGal distributes in the LT and QT along the BNS.

The map of the local anomaly (Fig. 6c) shows that positive and negative anomalies alternately occur from the Main Boundary Thrust to the Altyn Tagh fault. In the Pamir region, the northward arc with the alternate positive and negative anomalies is the major feature. Similarly, there is a northeastward bend with positive and negative anomalies on the southeastern margin of the Tibetan Plateau. The above two areas are located at the western and eastern ends of the Himalayas, i.e., the Western Himalayan Syntaxis and the Eastern Himalayan Syntaxis. Additionally, the negative anomalies cover the Tian Shan and Longmen Shan regions.

3. Methods

3.1. Moho inversion

The Parker-Oldenburg's algorithm (Parker, 1973; Oldenburg, 1974) was used for the Moho inversion in this study. Following Parker (1973), Oldenburg (1974) derived an iterative expression in the wave-number domain for the Moho relief $h(x,y)$ around the reference depth z_0,

$$F[h(x,y)] = -\frac{F[\Delta g(x,y)]e^{(-kz_0)}}{2\pi G\Delta\rho} - \sum_{n=2}^{\infty}\frac{k^{n-1}}{n!}F[h^n(x,y)] \quad (2)$$

where $\Delta g(x,y)$ is the gravity anomaly, $F[]$ is the Fourier transform; k is the wavenumber of the transformed function, and $\Delta\rho$ is the density contrast between the crust and the upper mantle. The details have been presented in previous studies (e.g. Gómez-Ortiz and Agarwal, 2005; Shin et al., 2006).

3.2. Crustal density inversion

In this study, the density anomaly is determined from the local gravity anomaly shown in Fig. 6c. The underground domain was divided into the fixed geometry of prisms, the densities of which are the undetermined parameters. The relationship between the gravity anomaly $\boldsymbol{G}$ and the density distribution $\boldsymbol{V}$ is.

$$\boldsymbol{G} = \boldsymbol{A}\boldsymbol{V} + \boldsymbol{E} \quad (3)$$

where $\boldsymbol{A}$ is the kernel matrix, and $\boldsymbol{E}$ is the noise associated with the gravity data. The principle of compact gravity inversion (Barbosa and

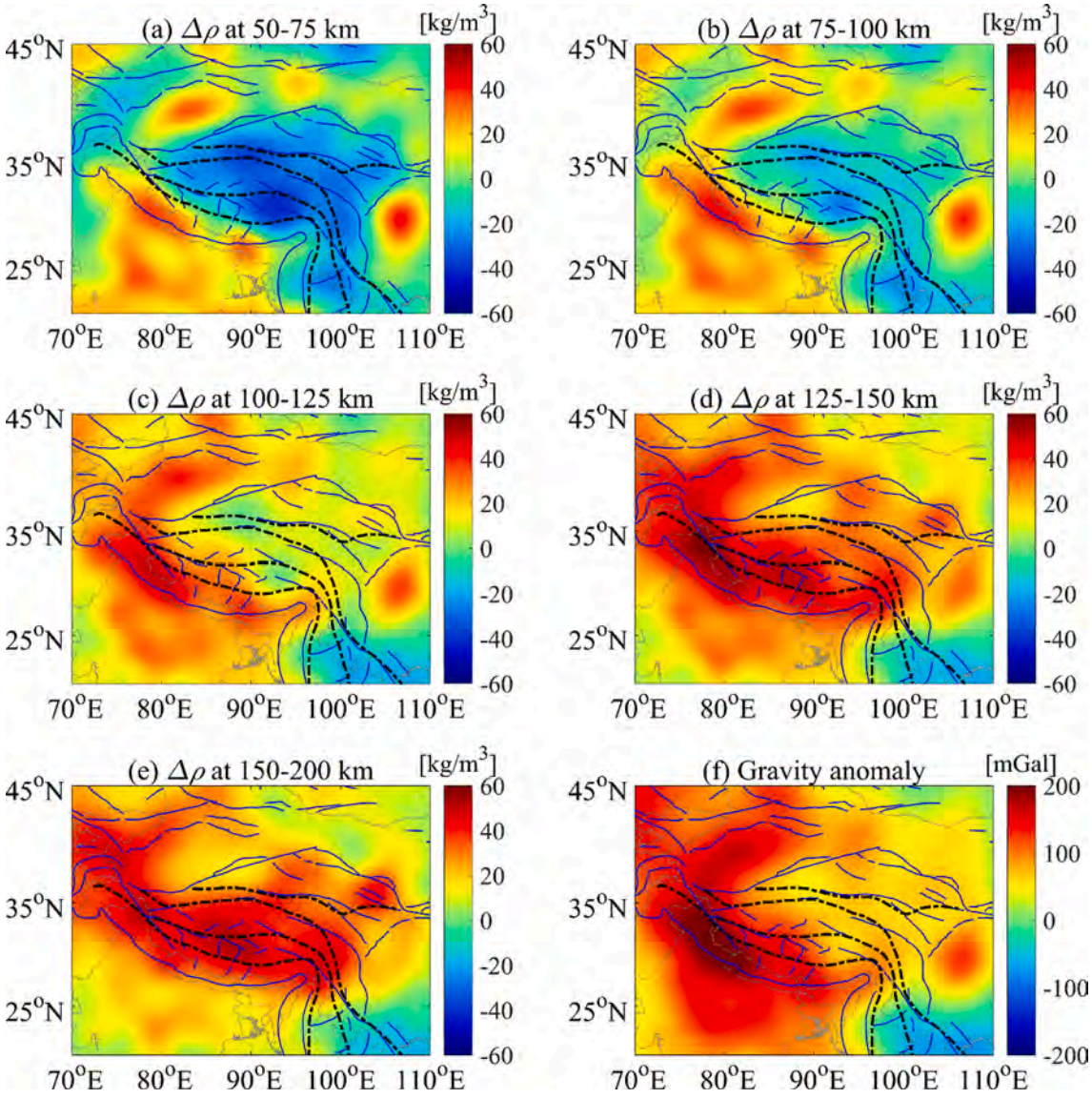

Fig. 5. (a-e) Density anomaly estimated from *Vs* structure shown in Fig. 4. (f) Gravity anomaly of the sum of anomalies derived from density anomalies shown in (a-e).

Silva, 1994; Last and Kubik, 1983) is to minimize the function of the density and noise as follows:

$$\sum_{j=1}^{M} w_{vj} v_j^2 + \sum_{i=1}^{N} w_{ei} e_i^2 \rightarrow \min \tag{4}$$

subject to Eq. (3). w_{vj} and w_{ei} are the weighting functions of the densities and gravity data, respectively. Following the method of Last and Kubik (1983), the solution of Eq.(3) can be expressed as.

$$\boldsymbol{V} = \boldsymbol{V}_0 + \boldsymbol{W}_v^{-1}\boldsymbol{A}^T\left(\boldsymbol{A}\boldsymbol{W}_v^{-1}\boldsymbol{A}^T + \boldsymbol{W}_e^{-1}\right)^{-1}\boldsymbol{G} \tag{5}$$

where $\boldsymbol{W}_v$ and $\boldsymbol{W}_e$ are composed of w_{vj} andw_{ei}, respectively. (Last and Kubik, 1983) defined$\boldsymbol{W}_e^{-1} = \ell_0^2 \mathrm{diag}\left(\mathbf{A}\mathbf{W}_v^{-1}\mathbf{A}^{\mathrm{T}}\right)$, where ℓ_0 is the priori estimated noise/signal ratio. The solution can be obtained directly from Eq. (5) for any initial model$\boldsymbol{V}_0$. In this study, the iteration started with $\boldsymbol{W}_v = \boldsymbol{I}$ and$\boldsymbol{V}_0 = 0$. The details of this method have been presented in previous articles (Barbosa and Silva, 1994; Last and Kubik, 1983).

It is known that the kernel matrix $\boldsymbol{A}$ decays with the inverse squared depth. To overcome the high sensitivity of the prisms near the surface, a depth-weighting matrix $\boldsymbol{W}_d$ is required (Boulanger and Chouteau, 2001; Chasseriau and Chouteau, 2003; Li and Oldenburg, 1998). We used $(\boldsymbol{W}_d)_{ii} = 1/(z_i + \varepsilon)^{\beta}$ and $\beta = 0.85$, which is consistent with the value of 0.85 used by Boulanger and Chouteau (2001) and is close to the value of 0.9 used by Chasseriau and Chouteau (2003). Then, Eq.(5) can be modified as follows:

$$\boldsymbol{V} = \boldsymbol{V}_0 + \boldsymbol{W}_d^{-1}\boldsymbol{W}_v^{-1}\boldsymbol{W}_d^{-1}\boldsymbol{A}^T\left(\boldsymbol{A}\boldsymbol{W}_d^{-1}\boldsymbol{W}_v^{-1}\boldsymbol{W}_d^{-1}\boldsymbol{A}^T + \boldsymbol{W}_e^{-1}\right)^{-1}\boldsymbol{G} \tag{6}$$

This method was applied to determine the crustal density change before the 2016 Menyuan earthquake. The numerical test for the availability is available in the supplementary file of Xuan et al. (2019).

4. Results and analysis

4.1. Moho topography

The parameters reference depth and density contrast should be known before deriving $h(x, y)$ in Eq. (2). Regarding the above group, the values are not really constants. The spectral analysis shown in Fig. 7 suggests 42.3 km can be considered as the reference depth. The Moho depth with varying reference depths of 30–60 km and density contrasts

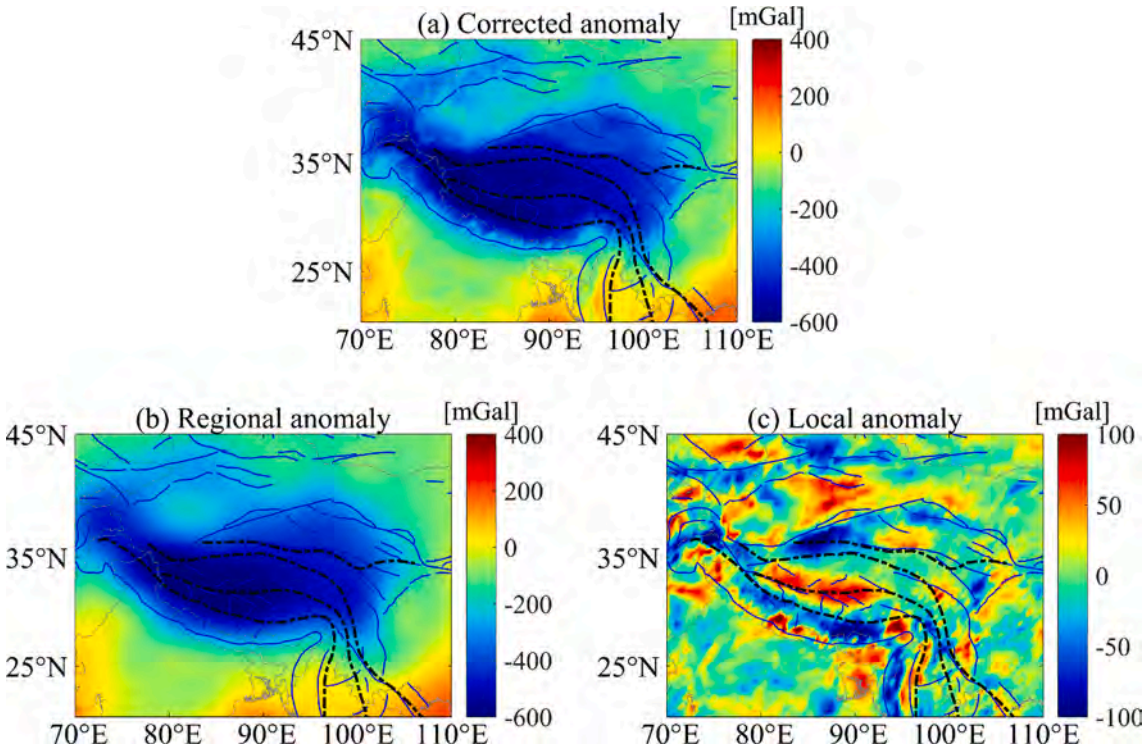

Fig. 6. Gravity anomalies in the Tibetan Plateau and its surroundings. (a) Corrected gravity anomaly. (b) Regional anomaly and (c) local anomaly.

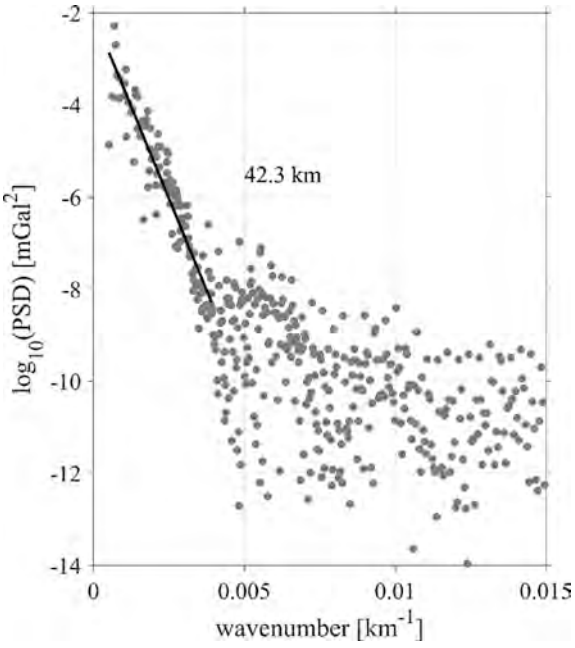

Fig. 7. Power spectral density (PSD) of the regional anomaly shown in Fig. 5c. The slop in black estimated the source depth of 42.3 km according to the relation between logarithm power spectrum and source depth.

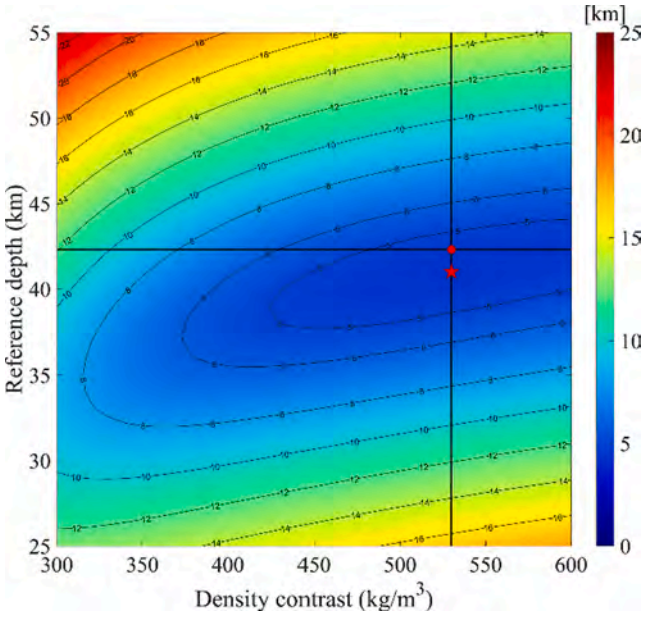

Fig. 8. RMS between the Moho depth from the gravity inversion and that of Li et al. (2014). The red star marks the RMS minimum of 4.38 km with reference depth of 41.0 km and density contrast of 530 kg/m^3. (For interpretation of the references to colour in this figure legend, the reader is referred to the web version of this article.)

of 300–600 kg/m^3 was computed, and then, the results were compared to that of Li et al. (2014) for determining the density contract.. Fig. 8 shows that the minimum of the root-mean-square (RMS) is 4.4 km with a reference level of 41 km and a density contrast of 530 kg/m^3 (red star in Fig. 8). When the reference depth of 42.3 km determined above is applied, the RMS is 4.5 km (red circle in Fig. 8). Therefore, the density contrast of 530 kg/m^3 is also suitable for inversion. To weaken the boundary effect, the inversion area was set as 60°E–120°E and 10°N–55°N, which is 10 degrees wider on each side than the study area (70°E–110°E and 20°N–45°N). After three iterations, the RMS correction of the Moho depth with respect to the previous iteration was only 19.8 m. The Moho depth and its gravity effect are shown in Fig. 8.

The inverted Moho depth (Fig. 9a) deeper than 50 km covers the Tibetan and Pamir plateaus, while the maximum depth of 75.1 km occurs beneath the BNS in the central Tibetan Plateau, corresponding to

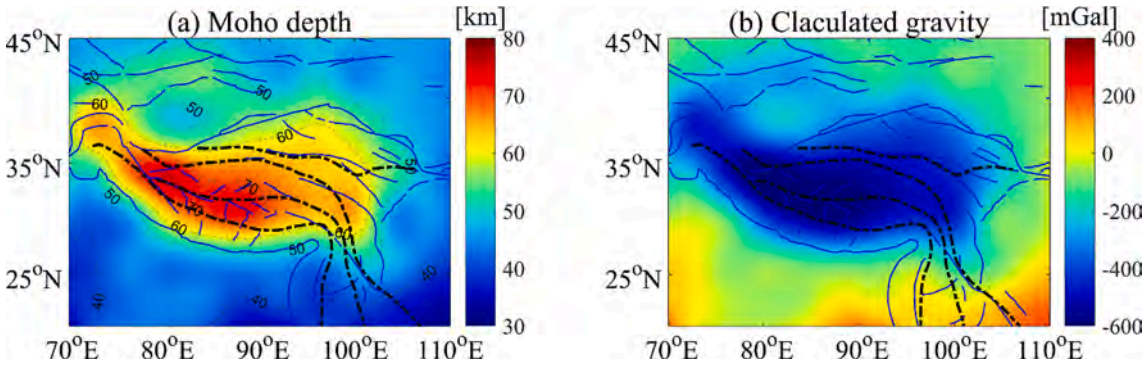

Fig. 9. Gravity-derived Moho depth and its gravity anomaly. (a) Moho depth inverted from the regional gravity anomaly shown in Fig. 6c. (b) Calculated gravity anomaly.

the seismic Moho (e.g. Zhang et al., 2014; Teng et al., 2020). The Moho is deeper than 70 km in the western LT and QT; however, it is ~60 km throughout the eastern Tibetan Plateau. Along the Indian subduction zone, the Moho depth exhibits a narrow gradient belt and increases linearly from 40 km to 70 km with an angle of about ~8.5°, and the relatively wider gradient belt is consistent with the smaller angle underneath the western and eastern ends of the Himalaya Mountains. The Moho depths of the tectonic units around Tibetan Plateau are not the

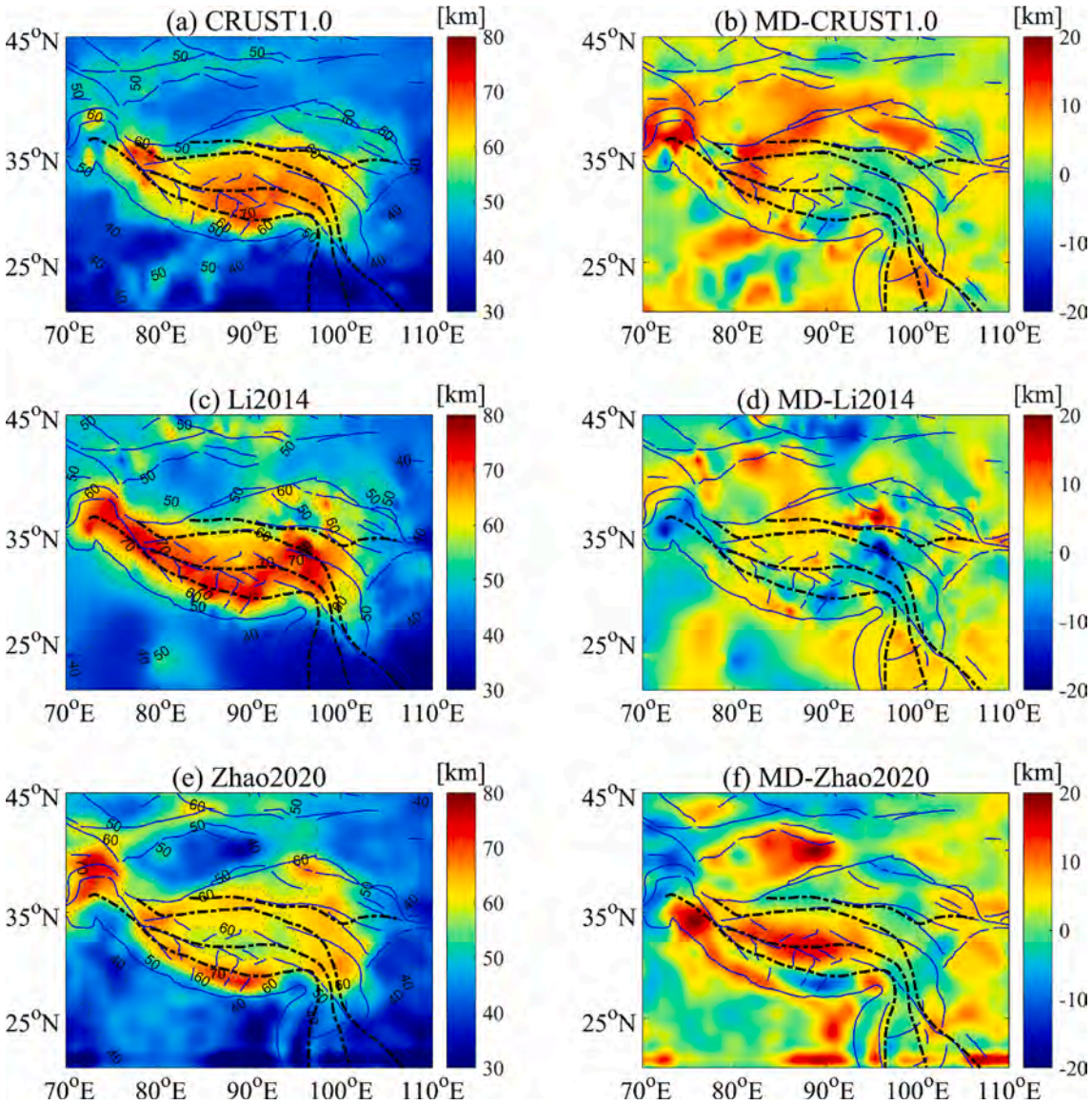

Fig. 10. (a, c, e) Moho depth of CRUST1.0 (Laske et al., 2013), Li2014 (Li et al., 2014) and Zhao2020 (Zhao et al., 2020). (b, d, f) Depth differences between this study (MD) and (a, c and e).

consistent with that of the plateau, i.e., a depth of ~40 km under the Indian Plate, ~50 km beneath the Tarim basin, and about 40 km beneath the Sichuan Basin. The Pamir region, northwest of the Tibetan Plateau, has a deeper Moho with a maximum depth of 60 km; and the Tian Shan region, north of the Tarim Basin, also has a deeper Moho depth of 50 km. It should also be noted that a Moho uplift of ~5 km occurs under the central part of the Tarim Basin.

Some features of our result are different from previous gravity-derived Moho depth (Braitenberg et al., 2000; Shin et al., 2007; Xu et al., 2017; Zhao et al., 2020). For comparison, the Moho from CRUST1.0 (Laske et al., 2013), the seismic Moho (Li et al., 2014) and the recent gravity-derived Moho (Zhao et al., 2020), as well as the differences are presented in Fig. 10. Moho depth from CRUST1.0 (Fig. 10a) shows the deepest Moho (~70 km) is observed in the middle LT, and the shallower Moho (50–60 km) in the northwestern Tibetan Plateau and Pamir region. Fig. 10b shows our Moho depth is deeper than that of CRUST1.0 (greater than10 km) in the northwestern Tibet, eastern Tarim basin and Pamir region. The seismic Moho depth shown in Fig. 10c presents deepest Moho exceeding 80 km is found in the eastern Tibetan Plaeau. However, the depth difference from our results (Fig. 10d) is less than 5 km in the study region, except some local area. As shown Fig. 10e, the deepest Moho is observed in the Pamir region reported by Zhao et al, (2020). Our Moho depth deeper than that of Zhao et al., (2020) is found in the eastern Tarim basin, LT and QT along the BNS in western Tibet, as well as the western HM. It is worth noting that the three deep belts in the Tibetan Plateau reported by Shin et al. (2007) and Zhao et al. (2020) were not found from Li et al. (2014) and this study. Additionally, this feature is also not reported in the seismic studies (e.g. Li et al., 2006; Li et al., 2014; Teng et al., 2020). We found that our gravity-inverted Moho depth (Fig. 9a) has good agreement with that of Li et al. (2014) shown in Fig. 10c.

4.2. Density structure

We modeled the crustal density structure using the residual gravity anomaly based on the method described in Section 3.2. The regional anomaly (Fig. 6b) not only includes the information for the Moho undulation but also for the mean density anomaly of the layered crust. The subsurface region from surface to 100 km was divided into 10 layers with a 10 km interval. After 10 iterations, the layered density structure was shown in Fig. 10. The residuals have an average of 0.05 mGal and a standard deviation of 0.77 mGal (Fig. 12), suggesting that the density estimation is reliable.

Our density structure exhibits a distinct lateral variation in the Tibetan crust (Fig. 11). From the 20–30 km layer to the 40–50 km layer (Fig. 11c–e), there is a low-density belt in the Himalaya Mountains between ~80°E and ~92°E, which corresponds to the anomalous body with low-velocity (Monsalve et al., 2008; He et al., 2010; Basuyau et al., 2013) and low-density (Basuyau et al., 2013). However, Tiwari et al. (2006) argued that the lower crust presents high density inferred from the gravity modelling. In the 50–60 km layer and the 60–70 km layer (Fig. 11f–g), the local low-density is also significant in the eastern segment of the above-described belt. Nevertheless, the high-density anomalies are present in the 10–20 km layer along the Main Boundary Thrust (Fig. 11b), and alternate low- and high-density anomalies are presented in the 20–40 km layer (Fig. 11c and d). In the western LT and

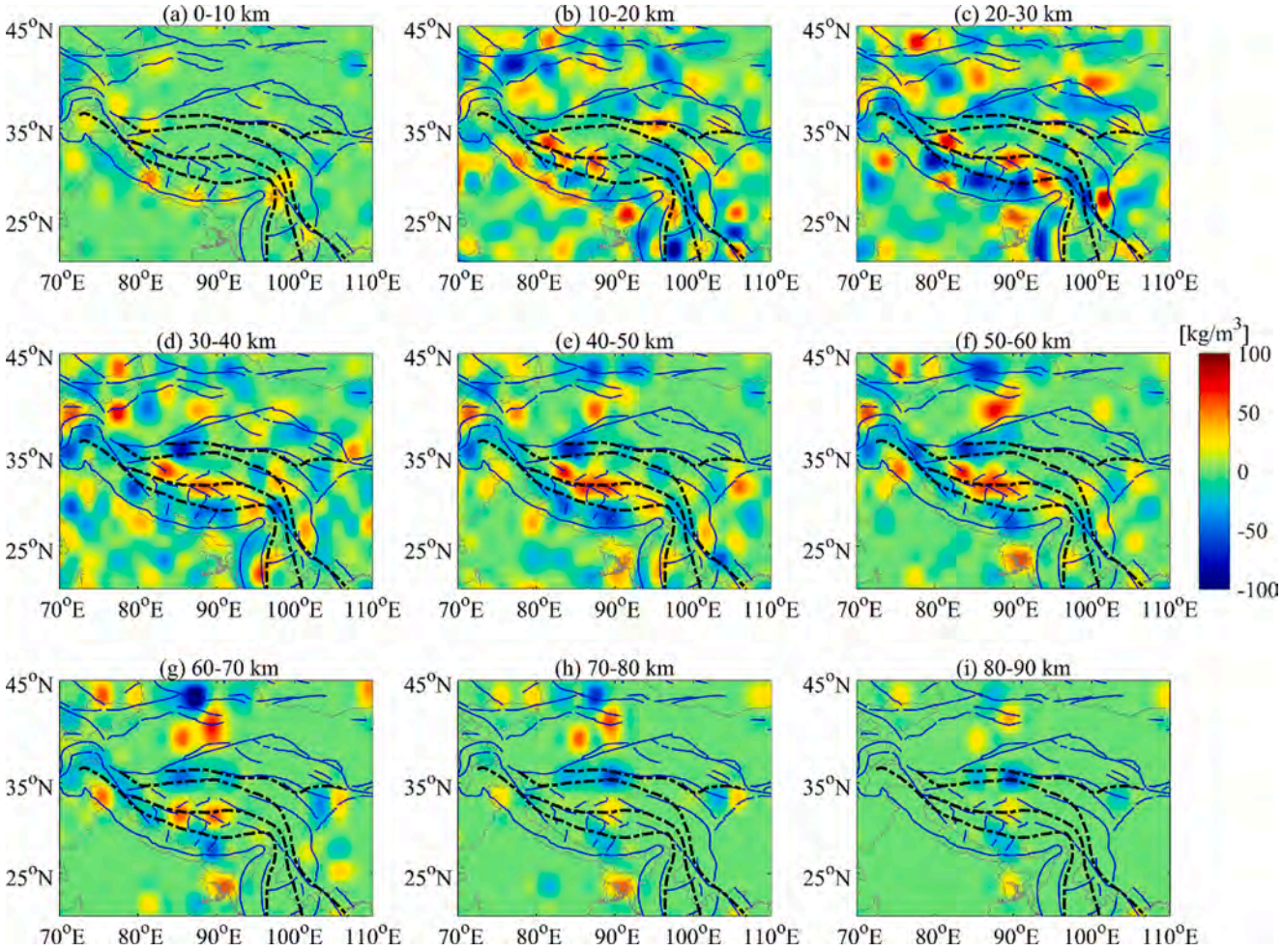

Fig. 11. The layered crustal density structure of the Tibetan Plateau and its surroundings.

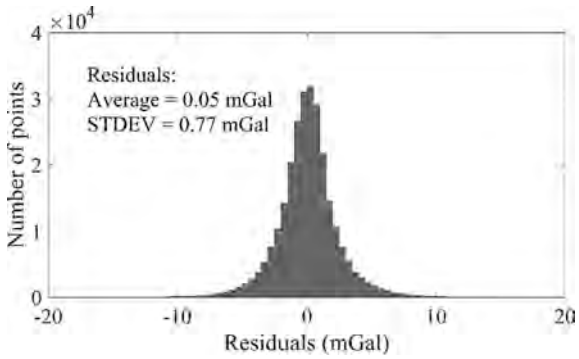

Fig. 12. Statistical analysis of final gravity residuals showed average of 0.05 mGal and standard deviation of 0.77 mGal.

QT, especially along the BNS, high-density anomalies are present in the 20–70 km layer (Fig. 11b–g). The main features of the density structures in above two belts are almost consistent with the densities from the joint inversion of the seismic and gravity data (Basuyau et al., 2013) and the velocities from the P-wave tomography (Zheng et al., 2007). Beneath the western ST and KT, on the northwestern part of the Tibetan Plateau, the low density anomalies dominate the entire crust, which is consistent with the argument of He et al. (2014) and the widespread low velocity anomaly in this region (Huang and Zhao, 2006; Zheng et al., 2007; Li et al., 2013; Liang et al., 2016).

In the Pamir region, a northward bending arc with a high density is present in the 10–20 km and 20–30 km layers on the north margin of the plateau. In contrast, a low-density anomaly appears in the plateau south of the high-density anomaly (Fig. 11b and c). Another significant feature is that the low-density anomaly is located at the junction of the Altyn Tagh and Karakoram faults from 20 to 60 km (Fig. 11c–f), where low resistivity values have been observed (Jin et al., 2010). On the south-eastern margin of the Tibetan Plateau, the two belts with low- and high-densities, in the 10–70 km layer and especially in the 20–50 km layer (Fig. 11c–e), are subparallel to each other forming a northeastward bulge. The high-density belt is approximately distributed along the IYS, while a narrow low-density belt is located along the BNS. This low-density belt is consistent with the low-resistivity (Bai et al., 2010) and the low-velocity anomaly (Li et al., 2016; Wu et al., 2016).

In the vertical section view of the N-S oriented section across the Tibetan Plateau (Fig. 13a), the main feature is the alternating low- and

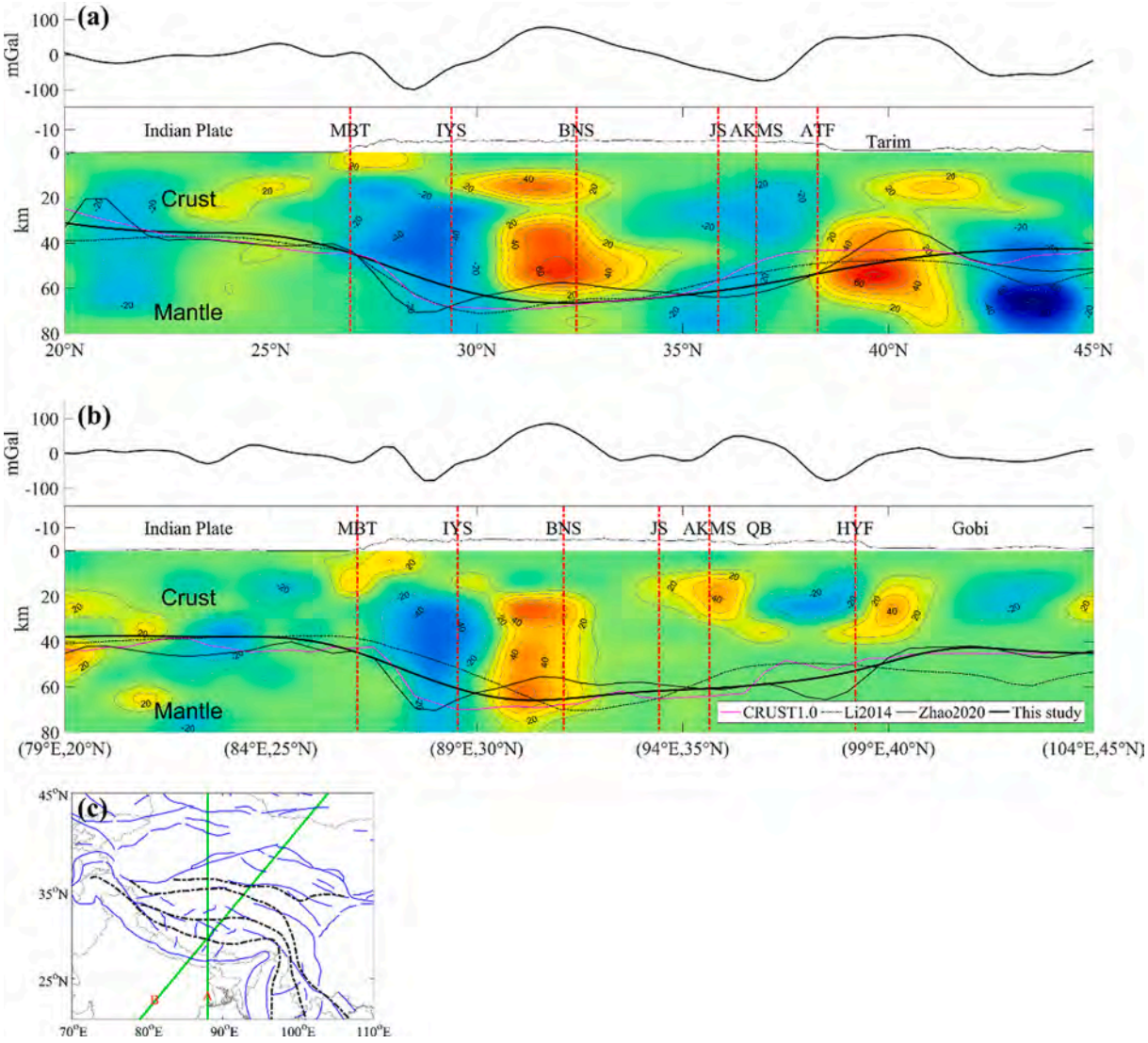

Fig. 13. Sections of the local gravity anomaly, density structure (in kg/m^3) and Moho depth across the Tibetan Plateau. (a) NS trend section A along 88°E. (b) NE-SW trend section B. (c) The green lines mark the locations of the two sections. *MBT*, Main Boundary thrust; *ATF*, Altyn Tagh fault; *HYF*, Haiyuan fault; *QB*, Qaidam Basin; other abbreviations are as in Fig. 1. (For interpretation of the references to colour in this figure legend, the reader is referred to the web version of this article.)

high-density anomalies between the Main Boundary Thrust to the south and the Altyn Tagh fault to the north. The top-down low density is mainly present in the Main Boundary Thrust area to the north of the IYS, which corresponds to the low-velocity anomaly (He et al., 2010; Zhang et al., 2014; Zheng et al., 2007), with its center located nearly at the Moho with a downward slope. A local high-density body exists in the lower crust and upper mantle between 31°N and 34°N, where the velocity is low (Zhang et al., 2014) and the Moho depth exceeds 70 km (Fig. 9a, 13a and b). However, this high-velocity anomaly does not extend to north of the BNS (He et al., 2010). To the north, there is a low-density body in the crust between the Jinsha suture and the Altyn Tagh fault, and there is another low-density body extending from the lower crust to the upper mantle. Two high-density bodies appear in the crust and mantle beneath the Tarim Basin, and there is a low-density anomaly in the upper mantle in the eastern part of the Tian Shan region. In the NE-SW trending section (Fig. 13b), the density anomalies between the Main Boundary Thrust and the BNS are similar to those in the N-S trending section. A relatively high-density anomaly exists in the upper crust beneath the Qaidam Basin and the AKMS, and a low-density anomaly exists beneath the Qilian Mountains, southwest of the Haiyuan fault.

5. Discussion

5.1. Crustal isostatic state inferred from the gravity Moho

Following Wang et al. (2009), the isostatic Moho depth can be determined from the elevation based on the Airy isostatic theory. The isostatic state of the crust can be inferred from the difference, i.e., by subtracting the isostatic Moho from our gravity Moho. A substitute of the above difference called the vertical tectonic stress is widely considered to be a quantitative measure of the isostatic state (Fu and She, 2017; Guy et al., 2017; Xuan et al., 2020). The vertical tectonic stress was calculated using the following formula: $P_v = -\rho_m g \Delta h$, where ρ_m is the mantle density, and g is the gravitational constant.

Fig. 14 shows the vertical tectonic stress in the Tibetan Plateau and surroundings. It is widely accepted that the Sichuan Basin is cold and strong (Clark and Royden, 2000; Copley and McKenzie, 2007; Teng et al., 2020), and mass balance is nearly achieved at the Moho where the tectonic stress is around 0 MPa (green), suggesting that our result is acceptable for investigating the isostatic state. The positive tectonic stress is mainly distributed in the marginal orogenic belts. In particular, it is greater than 40 MPa in the Himalayas, around 30 MPa along the Altyn Tagh and Qilian Mountains, and 50 MPa in the Longmen Shan region, suggesting that there is under-compensation in these regions. In most of the central part of the Tibetan Plateau, the vertical stress is −10 to 10 MPa; however, it is around −30 MPa in the Qaidam Basin and is around −10 MPa along the BNS, suggesting that a mass balance is roughly achieved at the Moho. The tectonic stress decreases gradually from about 30 MPa in the Indian Plate to about −20 MPa along the Main Boundary Thrust.

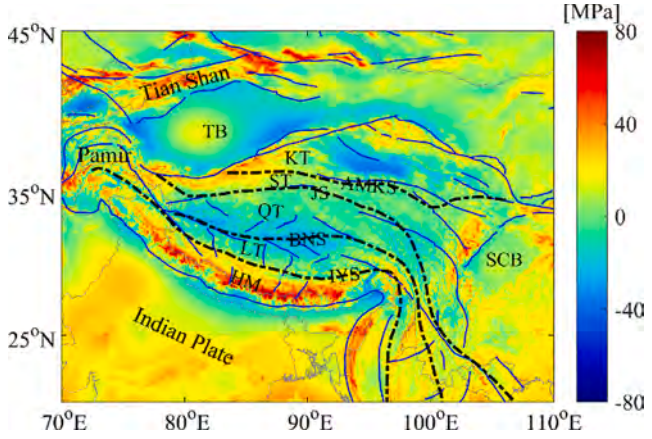

Fig. 14. Vertical tectonic stress in the Tibetan Plateau and its surroundings.

Alternatively, we assume that the mass balance is achieved at the lithospheric base following Gvirtzman and Nur (2001). In this way, the large tectonic stress underneath the HM (Fig. 14) can be compensated for by the thin lithospheric mantle, which can be verified by the receiver function images (Kumar et al., 2006; Tilmann et al., 2003) and the surface wave tomography (Zhang et al., 2014). On the contrary, the negative tectonic stress along the BNS corresponds to a relative thick lithospheric mantle; however, the seismic method reveals a thin lithosphere (Teng et al., 2020), which would be expained by mantle convection (Tilmann et al., 2003). Regarding the significantly low tectonic stress in the Qaidam Basin, a thick lithosphere is considered to balance it, which is in agreement with the seismic results (Teng et al., 2020; Zhang et al., 2014).

5.2. Tectonic implications

The Moho depth increases linearly northward between the Main Boundary to the south and 30°N to the north, suggesting that the rigid Indian Plate thrusts downward underneath the Tibetan Plateau, although the dip angle of about 8.5° along sections A and B (Fig. 7a and b) is less than the 10° dip angle obtained from the surface wave tomography (Zhang et al., 2014) and the 16.7° dip angle obtained from the gravity modeling (Bai et al., 2013). If there is underlying thin lithospheric mantle as the isostatic analysis, the Indian crust should be injected into the Tibetan lower crust (Owens and Zandt, 1997; Zhao and Morgan, 1984). The deepest Moho observed under the BNS suggests the Tibetan crust is underthrust resulted from the northward subducting Indian lithosphere and the southward subducting Asian lithosphere (Zhao et al., 2011).

Based on the views of previous studies and our results, we constructed the following possible scenario. The Indian crust has been injected into the Tibetan Plateau with small angle and has thickened the Tibetan crust, whereas the Indian lithospheric mantle is subducting under the Asian lithosphere. The dense lithosphere sinks at the subduction zone due to its negative buoyancy (Chen et al., 2020; Stern, 2007), which allows for the delamination of the subducting lithospheric mantle from the crust, causing downwelling. The suction induced by the subducting slab principally results in mantle convection on both sides of the slab (Conrad and Lithgow-Bertelloni, 2004). If the downwelling of the Indian lithospheric mantle with large angle occurs beneath the HM, the thin lithospheric mantle caused by the upwelling of the asthenosphere will occur to the north of the subducting lithospheric mantle, which is in agreement with the low-velocity anomaly reported by the seismic studies (Liang et al., 2016; Zhang et al., 2014). It is likely that the deepest Moho appears underneath the BNS (Fig. 6), which suggests that the Indian lithosphere extends to nearly the BNS and moves sharply downward, that is, at ~32°N as mentioned by Tilmann et al. (2003).

The low-density anomaly beneath the IYS (Figs. 12 and 13) is due to crustal shortening and partial melting caused by the India-Eurasia collision (Tilmann et al., 2003). Seismic studies have revealed a low-velocity anomaly in this region (Tilmann et al., 2003; Zheng et al., 2007; Monsalve et al., 2008; He et al., 2010; Basuyau et al., 2013; Liang et al., 2016). Additionally, this also provides evidence for absence of eclogites in the lower crust beneath the HM, which is in agreement with the results Bai et al. (2013) obtained from gravity modelling. The eclogite would not be formed in the conditions of a relatively cold plate underthrusting at a fast rate (Henry et al., 1997).

The low-density anomaly in the lower-crust and upper-mantle underneath the JS in section A (Fig. 13a) corresponded to the widely exhibiting low-velocity anomalies (Huang and Zhao, 2006; Zheng et al., 2007; Li et al., 2013; Liang et al., 2016). The low-density anomaly may be related to the ultrapotassic volcanics (He et al., 2014). However, this

feature is absent in section B (Fig. 13b). Section B nearly overlaps with the eastern margin of the metasomatized lid found in the seismic study of (Zhang et al., 2014), suggesting that the upwelling of the asthenosphere under the QT and ST occurs to the west of ~94°E and the Indian Plate extends to different distances (Liang et al., 2016; Zhang et al., 2014). The upwelling of the asthenosphere can be suggested by the Moho map (Fig. 9a). The upwelling asthenosphere in this region is possibly due to the asthenospheric convection caused by the downwelling of the subducting Indian Plate (Conrad and Lithgow-Bertelloni 2004).

On the southeastern margin of the Tibetan Plateau, the *en echelon* pattern of the low- and high-density anomalies (Fig. 11b–e) corresponds to the western channel of lower crustal flow inferred from the magnetotelluric images (Bai et al., 2010) and the seismic images (Li et al., 2016; Wu et al., 2016). Xuan et al. (2016) argued that the folded crust existed in this region resulting from the combination of the southeastward extrusion of the Tibetan Plateau and the subducting Indian Plate.

6. Conclusions

In this study, we determined the Moho depth and crustal density structure of the Tibetan Plateau and its surroundings using inverse modelling of the gravity data. After correcting the gravity effects from sediments and upper mantle, the separated regional and local anomalies were arranged to invert the Moho undulation and density perturbation, respectively.

The main crustal features were imaged, such as the sublinearly of the Moho increasing underneath the southern part of the Tibetan Plateau, the lateral variations in the density in the central and western parts of the Tibetan Plateau, and the probable presence and absence of eclogites beneath the Himalaya, Lhasa, and Qiangtang terranes. To accommodate the convergence of the subducting Indian and Asian lithosphere, the Tibetan crust beneath BNS presents underthrust (Zhao et al., 2011) and Moho depth exceeds 70 km. The increasing Moho depth from south to north is probably due to the negative buoyancy of the underthrusting Indian Plate, which would induce the local mantle convection under the southern and northern parts of the underthrusting plate (Tilmann et al., 2003). The upwelling asthenospheric materials are considered to be the main reason for the thin lithosphere underlying the Himalayas and the low-density anomaly underneath the northern part of the Tibetan Plateau.

CRediT authorship contribution statement

Songbai Xuan: Visualization, Software, Data curation, Investigation, Writing – original draft. **Shuanggen Jin:** Conceptualization, Methodology, Writing – review & editing, Validation.

Declaration of Competing Interest

The authors declare that they have no known competing financial interests or personal relationships that could have appeared to influence the work reported in this paper.

Acknowledgments

We would like to thank Associate Editor Dr. Vineet Kumar Gahalaut and two anonymous reviewers for their constructive and helpful reviews. This work was supported by the National Natural Science Foundation of China (Grant No. 42074090), the National Key Research and Development Program of China Project (Grant No. 2018YFC0603502 and 2021YFA0716100).

References

Bai, D., Unsworth, M.J., Meju, M.A., Ma, X., Teng, J., Kong, X., Sun, Y.i., Sun, J., Wang, L., Jiang, C., Zhao, C., Xiao, P., Liu, M., 2010. Crustal deformation of the eastern Tibetan plateau revealed by magnetotelluric imaging. Nat. Geosci. 3 (5), 358–362.

Bai, Z., Zhang, S., Braitenberg, C., 2013. Crustal density structure from 3D gravity modeling beneath Himalaya and Lhasa blocks, Tibet. J. Asian Earth Sci. 78, 301–317.

Bao, X., Song, X., Li, J., 2015. High-resolution lithospheric structure beneath Mainland China from ambient noise and earthquake surface-wave tomography. Earth Planet. Sci. Lett. 417, 132–141.

Barbosa, V.C.F., Silva, J.B.C., 1994. Generalized compact gravity inversion. Geophysics 59 (1), 57–68.

Basuyau, C., Diament, M., Tiberi, C., Hetenyi, G., Vergne, J., Peyrefitte, A., 2013. Joint inversion of teleseismic and GOCE gravity data: application to the Himalayas. Geophys. J. Int. 193 (1), 149–160.

Bonvalot, S., Balmino, G., Briais, A., Kuhn, M., Peyrefitte, A., Vales, N., Biancale, R., Gabalda, G., Reinquin, F., Sarrailh, M., 2012. World Gravity Map. In: BGI-CGMW-CNES-IRD (Editor), Commission for the Geological Map of the World, Paris.

Boulanger, O., Chouteau, M., 2001. Constraints in 3D gravity inversion. Geophys. Prospect. 49 (2), 265–280.

Braitenberg, C., Zadro, M., Fang, J., Wang, Y., Hsu, H.T., 2000. Gravity inversion in Qinghai-Tibet plateau. Physics and Chemistry of the Earth Part A-Solid Earth and Geodesy 25 (4), 381–386.

Chasseriau, P., Chouteau, M., 2003. 3D gravity inversion using a model of parameter covariance. J. Appl. Geophys. 52 (1), 59–74.

Chen, L., Wang, X.u., Liang, X., Wan, B.o., Liu, L., 2020. Subduction tectonics vs. Plume tectonics-Discussion on driving forces for plate motion. Sci. China Earth Sci. 63 (3), 315–328.

Clark, M.K., Royden, L.H., 2000. Topographic ooze: Building the eastern margin of Tibet by lower crustal flow. Geology 28, 703–706.

Conrad, C.P., Lithgow-Bertelloni, C., 2004. The temporal evolution of plate driving forces: Importance of "slab suction" versus "slab pull" during the Cenozoic. J. Geophys. Res. Solid Earth 109 (B10). https://doi.org/10.1029/2004JB002991.

Copley, A., McKenzie, D., 2007. Models of crustal flow in the India-Asia collision zone. Geophys. J. Int. 169 (2), 683–698.

Deng, Y.F., Fan, W.M., Zhang, Z.J., Liang, K., 2014. The gravity and isostatic Moho in North China Craton and their implication to seismicity. Earthq. Sci. 27 (2), 197–207.

Deng, Y., Levandowski, W., Kusky, T., 2017. Lithospheric density structure beneath the Tarim basin and surroundings, northwestern China, from the joint inversion of gravity and topography. Earth Planet. Sci. Lett. 460, 244–254.

Fu, G., She, Y., 2017. Gravity Anomalies and Isostasy Deduced From New Dense Gravimetry Around the Tsangpo Gorge, Tibet. Geophys. Res. Lett. 44 (20), 10,233–10,239.

Gómez-Ortiz, D., Agarwal, B.N.P., 2005. 3DINVER.M: a MATLAB program to invert the gravity anomaly over a 3D horizontal density interface by Parker-Oldenburg's algorithm. Comput. Geosci. 31 (4), 513–520.

Guy, A., Holzrichter, N., Ebbing, J., 2017. Moho depth model for the Central Asian Orogenic Belt from satellite gravity gradients. J. Geophys. Res. Solid Earth 122 (9), 7388–7407.

Gvirtzman, Z., Nur, A., 2001. Residual topography, lithospheric structure and sunken slabs in the central Mediterranean. Earth Planet. Sci. Lett. 187 (1-2), 117–130.

He, R., Zhao, D., Gao, R., Zheng, H., 2010. Tracing the Indian lithospheric mantle beneath central Tibetan Plateau using teleseismic tomography. Tectonophysics 491 (1-4), 230–243.

He, R., Liu, G., Golos, E., Gao, R., Zheng, H., 2014. Isostatic gravity anomaly, lithospheric scale density structure of the northern Tibetan plateau and geodynamic causes for potassic lava eruption in Neogene. Tectonophysics 628, 218–227.

Henry, P., Le Pichon, X., Goffé, B., 1997. Kinematic, thermal and petrological model of the Himalayas: Constraints related to metamorphism within the underthrust Indian crust and topographic elevation. Tectonophysics 273 (1-2), 31–56.

Hetényi, G., Cattin, R., Brunet, F., Bollinger, L., Vergne, J., Nábělek, J.L., Diament, M., 2007. Density distribution of the India plate beneath the Tibetan plateau: Geophysical and petrological constraints on the kinetics of lower-crustal eclogitization. Earth Planet. Sci. Lett. 264 (1-2), 226–244.

Houseman, G., England, P., 1986. Finite strain calculations of continental deformation 1. Method and general results for convergent zones. J. Geophys. Res. 91 (B3), 3651–3663.

Huang, J.L., Zhao, D.P., 2006. High-resolution mantle tomography of China and surrounding regions. J. Geophys. Res. Solid Earth 111 (B9). https://doi.org/10.1029/2005jb004066.

Jiménez-Munt, I., Fernàndez, M., Vergés, J., Platt, J.P., 2008. Lithosphere structure underneath the Tibetan Plateau inferred from elevation, gravity and geoid anomalies. Earth Planet. Sci. Lett. 267 (1-2), 276–289.

Jin, S., Wei, W.B., Wang, S., Ye, G.F., Deng, M., Tan, H.D., 2010. Discussion of the formation and dynamic signification of the high conductive layer in Tibetan crust. Chinese J. Geophys. 53 (10), 2376–2385.

Jin, S., Park, P.-H., 2006. Strain accumulation in South Korea inferred from GPS measurements. Earth Planets Space 58 (5), 529–534.

Jin, S.G., Zhang, L., Tapley, B., 2011. The understanding of length-of-day variations from satellite gravity and laser ranging measurements. Geophys. J. Int. 184 (2), 651–660.

Kumar, P., Yuan, X., Kind, R., Ni, J., 2006. Imaging the colliding Indian and Asian lithospheric plates beneath Tibet. J. Geophys. Res. Solid Earth 111 (B6). https://doi.org/10.1029/2005JB003930.

Kustowski, B., Ekström, G., Dziewoński, A.M., 2008a. The shear-wave velocity structure in the upper mantle beneath Eurasia. Geophys. J. Int. 174 (3), 978–992.
Kustowski, B., Ekström, G., Dziewoński, A.M., 2008b. Anisotropic shear-wave velocity structure of the Earth's mantle: A global model. J. Geophys. Res. 113, B06306. https://doi.org/10.1029/2007JB005169.
Laske, G., Masters., G., Ma, Z., Pasyanos, M., 2013. Update on CRUST1.0 - A 1-degree Global Model of Earth's Crust. Geophys. Res. Abstracts, 15: Abstract EGU2013-2658.
Last, B.J., Kubik, K., 1983. Compact gravity inversion. Geophysics 48 (6), 713–721.
Levandowski, W., Boyd, O.S., Briggs, R.W., Gold, R.D., 2015. A random-walk algorithm for modeling lithospheric density and the role of body forces in the evolution of the Midcontinent Rift. Geochem. Geophys. Geosyst. 16 (12), 4084–4107.
Li, C., van der Hilst, R.D., Meltzer, A.S., Engdahl, E.R., 2008. Subduction of the Indian lithosphere beneath the Tibetan Plateau and Burma. Earth Planet. Sci. Lett. 274 (1-2), 157–168.
Li, M., Zhang, S., Wang, F., Wu, T., Qin, W., 2016. Crustal and upper-mantle structure of the southeastern Tibetan Plateau from joint analysis of surface wave dispersion and receiver functions. J. Asian Earth Sci. 117, 52–63.
Li, S., Mooney, W.D., Fan, J., 2006. Crustal structure of mainland China from deep seismic sounding data. Tectonophysics 420 (1-2), 239–252.
Li, Y., Oldenburg, D.W., 1998. 3-D inversion of gravity data. Geophysics 63 (1), 109–119.
Li, Y., Gao, M., Wu, Q., 2014. Crustal thickness map of the Chinese mainland from teleseismic receiver functions. Tectonophysics 611, 51–60.
Li, Y., Wu, Q., Pan, J., Zhang, F., Yu, D., 2013. An upper-mantle *S*-wave velocity model for East Asia from Rayleigh wave tomography. Earth Planet. Sci. Lett. 377-378, 367–377.
Liang, X., Chen, Y., Tian, X., Chen, Y.J., Ni, J., Gallegos, A., Klemperer, S.L., Wang, M., Xu, T., Sun, C., Si, S., Lan, H., Teng, J., 2016. 3D imaging of subducting and fragmenting Indian continental lithosphere beneath southern and central Tibet using body-wave finite-frequency tomography. Earth Planet. Sci. Lett. 443, 162–175.
Molnar, P., Tapponnier, P., 1975. Cenozoic tectonics of Asia: Effects of a continental collision. Science 189, 419–426.
Monsalve, G., Sheehan, A., Rowe, C., Rajaure, S., 2008. Seismic structure of the crust and the upper mantle beneath the Himalayas: Evidence for eclogitization of lower crustal rocks in the Indian Plate. J. Geophys. Res. Solid Earth 113 (B08315). https://doi.org/10.1029/2007JB005424.
Nábělek, J., Hetényi, G., Vergne, J., Sapkota, S., Kafle, B., Jiang, M., Su, H., Chen, J., Huang, B.-S., Team, T.-CLIMB., 2009. Underplating in the Himalaya-Tibet Collision Zone Revealed by the Hi-CLIMB Experiment. Science 325 (5946), 1371–1374.
Oldenburg, D.W., 1974. The inversion and interpretation of gravity anomalies. Geophysics 39 (4), 526–536.
Owens, T.J., Zandt, G., 1997. Implications of crustal property variations for models of Tibetan plateau evolution. Nature 387 (6628), 37–43.
Parker, R.L., 1973. The rapid calculation of potential anomalies. Geophys. J. R. Astron. Soc. 31 (4), 447–455.
Royden, L.H., Burchfiel, B.C., King, R.W., Wang, E., Chen, Z., Shen, F., Liu, Y., 1997. Surface deformation and lower crustal flow in eastern Tibet. Science 276 (5313), 788–790.
Sato, H., Sacks, I.S., Murase, T., 1989. The use of laboratory velocity data for estimating temperature and partial melt fraction in the low-velocity zone_ Comparison with heat flow and electrical conductivity studies. J. Geophys. Res. 94 (B5), 5689–5704.
Shin, Y.H., Choi, K.S., Xu, H., 2006. Three-dimensional forward and inverse models for gravity fields based on the Fast Fourier Transform. Comput. Geosci. 32 (6), 727–738.
Shin, Y.H., Xu, H., Braitenberg, C., Fang, J., Wang, Y., 2007. Moho undulations beneath Tibet from GRACE-integrated gravity data. Geophys. J. Int. 170 (3), 971–985.
Stern, R.J., 2007. When and how did plate tectonics begin? Theoretical and empirical considerations. Chin. Sci. Bull. 52 (5), 578–591.
Tapponnier, P., Peltzer, G., Le Dain, A.Y., Armijo, R., Cobbold, P., 1982. Propagating extrusion tectonics in Asia: New insights from simple experiments with plasticine. Geology 10 (12), 611–616.
Teng, J.W., Yang, D.H., Tian, X.B., Xu, T., Chen, Y., Bai, Z.M., Liang, X.F., Zhang, X., Wu, J., Liu, S.Y., 2020. Geophysical investigation progresses of the Qinghai-Tibetan Plateau in the past 70 years. Scientia Sinica Terrae 49, 1546–1564.
Teng, J., Zhang, Z., Zhang, X., Wang, C., Gao, R., Yang, B., Qiao, Y., Deng, Y., 2013. Investigation of the Moho discontinuity beneath the Chinese mainland using deep seismic sounding profiles. Tectonophysics 609, 202–216.
Tenzer, R., Chen, W., Jin, S.G., 2015. Effect of the upper mantle density structure on the Moho geometry. Pure Appl. Geophys. 172 (6), 1563–1583.
Tilmann, F., Ni, J., Seismic Team, 2003. Seismic imaging of the downwelling Indian lithosphere beneath central Tibet. Science 300 (5624), 1424–1427.
Tiwari, V., Vyghreswararao, M., Mishra, D., Singh, B., 2006. Crustal structure across Sikkim, NE Himalaya from new gravity and magnetic data. Earth Planet. Sci. Lett. 247 (1-2), 61–69.
Wang, Q.S., Teng, J.W., Zhang, Y.Q., Zhang, X.M., Yang, H., 2009. The crustal structure and gravity isostasy in the middle western Sichuan area. Chinese J. Geophys. 52 (2), 579–583.
Wang, Y.X., Mooney, W.D., Yuan, X.C., Coleman, R.G., 2003. The crustal structure from the Altai mountains to the Altyn Tagh fault, northwest China. J. Geophys. Res. Solid Earth 108 (B6). https://doi.org/10.1029/2001jb000552.
Wang, Z., Zhao, D., Gao, R., Hua, Y., 2019. Complex subduction beneath the Tibetan plateau: A slab warping model. Phys. Earth Planet. Inter. 292, 42–54.
Wu, T., Zhang, S., Li, M., Qin, W., Zhang, C., 2016. Two crustal flowing channels and volcanic magma migration underneath the SE margin of the Tibetan Plateau as revealed by surface wave tomography. J. Asian Earth Sci. 132, 25–39.
Xu, C., Liu, Z., Luo, Z., Wu, Y., Wang, H., 2017. Moho topography of the Tibetan Plateau using multi-scale gravity analysis and its tectonic implications. J. Asian Earth Sci. 138, 378–386.
Xuan, S., Jin, S.G., Chen, Y., 2020. Determination of the isostatic and gravity Moho in the East China Sea and its implications. J. Asian Earth Sci. 187 (1), 104098 https://doi.org/10.1016/j.jseaes.2019.104098.
Xuan, S., Jin, S.G., Chen, Y., Wang, J.P., 2019. Insight into the preparation of the 2016 M_S6.4 Menyuan earthquake from terrestrial gravimetry-derived crustal density changes. Sci. Rep. 9, 18227. https://doi.org/10.1038/s41598-019-54581-5.
Xuan, S., Shen, C., Li, H., Tan, H., 2016. Structural interpretation of the Chuan-Dian block and surrounding regions using discrete wavelet transform. Int. J. Earth Sci. 105 (5), 1591–1602.
Yang, W.C., Shi, Z.Q., Hou, Z.Z., Cheng, Z.Y., 2001. Discrete wavelet transform for multiple decomposition of gravity anomalies. Chinese J. Geophys. 44 (4), 534–545.
Yin, A., Harrison, T.M., 2000. Geologic evolution of the Himalayan-Tibetan orogen. Annu. Rev. Earth Planet. Sci. 28 (1), 211–280.
Zhang, Z., Teng, J., Romanelli, F., Braitenberg, C., Ding, Z., Zhang, X., Fang, L., Zhang, S., Wu, J., Deng, Y., Ma, T., Sun, R., Panza, G.F., 2014. Geophysical constraints on the link between cratonization and orogeny: Evidence from the Tibetan Plateau and the North China Craton. Earth Sci. Rev. 130, 1–48.
Zhao, G.D., Liu, J.X., Chen, B., Kaban, M.K., Zheng, X.Y., 2020. Moho beneath Tibet based on a joint analysis of gravity and seismic data. Geochem. Geophys. Geosyst. 21 (2) e2019GC008849.
Zhao, L.-F., Xie, X.-B., He, J.-K., Tian, X., Yao, Z.-X., 2013. Crustal flow pattern beneath the Tibetan Plateau constrained by regional Lg-wave Q tomography. Earth Planet. Sci. Lett. 383, 113–122.
Zhao, W.-L., Morgan, W.J., 1984. Injection of Indian crust into Tibetan lower crust: A two-dimensional finite element model study. Tectonics 6 (4), 489–504.
Zhao, W., Kumar, P., Mechie, J., Kind, R., Meissner, R., Wu, Z., Shi, D., Su, H., Xue, G., Karplus, M., Tilmann, F., 2011. Tibetan plate overriding the Asian plate in central and northern Tibet. Nat. Geosci. 4 (12), 870–873.
Zheng, H.-W., Li, T.-D., Gao, R., Zhao, D.-P., He, R.-Z., 2007. Teleseismic P-wave tomography evidence for the Indian lithospheric mantle subducting northward beneath the Qiangtang terrane. Chinese J. Geophys. 50 (5), 1223–1232.
Zhu, D.-C., Zhao, Z.-D., Niu, Y., Dilek, Y., Hou, Z.-Q., Mo, X.-X., 2013. The origin and pre-Cenozoic evolution of the Tibetan Plateau. Gondwana Res. 23 (4), 1429–1454.